water

Article

# Monitoring the Water Quality Distribution Characteristics in the Huaihe River Basin Based on the Sentinel-2 Satellite

**Xuanshuo Shi [1], Zhongfeng Qiu [1,2,*], Yunjian Hu [1], Dongzhi Zhao [1], Aibo Zhao [3], Hui Lin [4,5], Yating Zhan [1], Yu Wang [1] and Yuanzhi Zhang [1]**

1 School of Marine Sciences, Nanjing University of Information Science and Technology, Nanjing 210044, China; 20211237005@nuist.edu.cn (X.S.); 20211209004@nuist.edu.cn (Y.H.); 900232@nuist.edu.cn (D.Z.); zytayx@sina.com (Y.Z.); yuwang@nuist.edu.cn (Y.W.); yzhang209@nuist.edu.cn (Y.Z.)
2 Key Laboratory of Space Ocean Remote Sensing and Applications, Ministry of Natural Resources, Beijing 100081, China
3 Jiangsu Tidal Flat Research Center, Nanjing 210036, China; 13913309765@139.com
4 Fujian Provincial Key Laboratory of Severe Weather, Fujian Institute of Meteorological Science, Fuzhou 350007, China; zhtqsyslh@126.com
5 China Meteorological Administration Strait Key Open Laboratory of Severe Weather, Fujian Institute of Meteorological Science, Fuzhou 350007, China
* Correspondence: zhongfeng.qiu@nuist.edu.cn

**Abstract:** Remote sensing technology plays a crucial role in the rapid and wide-scale monitoring of water quality, which is of great significance for water pollution prevention and control. In this study, the downstream and nearshore areas of the Huaihe River Basin were selected as the study area. By utilizing spectral information from standard solution measurements in the laboratory and in situ water quality data matched with satellite spatiotemporal data, inversion models for total phosphorus (TP) and ammonia nitrogen ($NH_3$-N) water quality parameters were developed. The validation results using field measurements demonstrated that the inversion models performed well, with coefficients of determination ($R^2$) of 0.7302 and 0.8024 and root mean square errors of 0.02614 mg/L and 0.0368 mg/L for total phosphorus and ammonia nitrogen, respectively. By applying the models to Sentinel-2 satellite images from 2022, the temporal and spatial distribution characteristics of total phosphorus and ammonia nitrogen concentrations in the study area were obtained. The ammonia nitrogen concentration ranged from 0.05 to 0.30 mg/L, while the total phosphorus concentration ranged from 0.10 to 0.40 mg/L. Overall, the distribution appeared to be stable. The southern region of the Guan River estuary showed slightly higher water quality parameter concentrations compared to the northern region, while the North Jiangsu Irrigation Main Canal estuary was affected by the dilution of river water, resulting in lower concentrations in the estuarine area.

**Keywords:** Huaihe River Basin; water quality parameters; Sentinel-2; spatiotemporal distribution



**Citation:** Shi, X.; Qiu, Z.; Hu, Y.; Zhao, D.; Zhao, A.; Lin, H.; Zhan, Y.; Wang, Y.; Zhang, Y. Monitoring the Water Quality Distribution Characteristics in the Huaihe River Basin Based on the Sentinel-2 Satellite. *Water* **2024**, *16*, 860. https://doi.org/10.3390/w16060860

Academic Editor: Christos S. Akratos

Received: 25 January 2024
Revised: 8 March 2024
Accepted: 13 March 2024
Published: 16 March 2024



## 1. Introduction

The Huaihe River Basin is located in the northern part of Jiangsu Province. In recent years, with the acceleration of industrialization, large amounts of industrial wastewater and domestic sewage containing nutrients have been discharged into the Huaihe River. This has led to the increasingly severe eutrophication of the river [1]. The nutrient input from land sources has a significant impact on the water quality ecosystem of the estuarine area, such as the excessive proliferation of algae and other planktonic organisms. The excessive proliferation of algae consumes dissolved oxygen in the water, resulting in decreased oxygen levels. This makes it difficult for oxygen-demanding plants to survive and leads to a large number of fish and other organisms dying due to a lack of oxygen [2]. Conducting water quality monitoring in the Huaihe River Basin is helpful for understanding its spatiotemporal variations and gaining knowledge about the current status and changes in land-based nutrient inputs. It is also of great importance for pollution source tracing, water nutrient-carrying capacity assessment, and integrated land–sea management.

Of the water quality parameters, nitrogen and phosphorus contents are closely related to eutrophication and algae growth in water bodies. The water quality changes in the Huaihe River Basin were assessed and analyzed using data from 110 monitoring sections spanning 2003–2019 [3]. The results indicate a significant increase in pollution for total phosphorus (TP) in the downstream area of the Huaihe River. Since phosphorus is a major limiting factor for eutrophication, this suggests a growing risk of blue-green algal blooms in downstream water bodies. Conversely, the ammonia nitrogen ($NH_3$-N) indicator exhibited a clear downward trend. Total phosphorus and ammonia nitrogen are important water quality parameters in this regard. Ammonia nitrogen directly stimulates the proliferation of algae, while total phosphorus encompasses the collective influence of all phosphorus forms on water quality. Previous research has established total phosphorus and ammonia nitrogen as indicators for elucidating nutrient pollution, with agricultural activities identified as the primary source of nutrient pollution in surface water [4,5]. Compared to the traditional on-site monitoring of total phosphorus and ammonia nitrogen, remote sensing technology provides a fast and wide-ranging means of obtaining the spatial and temporal distribution characteristics of water quality parameters. Numerous researchers have utilized different sensor data, such as MODIS and GOCI, to conduct remote sensing inversion studies on water quality parameters, including total phosphorus, total nitrogen, and ammonia nitrogen [6–17].

Remote sensing technology provides an accurate synoptic view of water quality indices (WQIs) due to its strengths in extended spatial and temporal coverage [18]. Remote sensing satellites, such as Landsat-8, Sentinel-2, MODIS, VIIRS, and others, are equipped with sensors that cover the visible and near-infrared spectra. These satellites have the capability of estimating concentrations of chlorophyll-a (Chla); colored, dissolved organic matter (CDOM); Secchi disk depth (SDD); turbidity; total suspended matter (TSM); water temperature (WT); TP; sea surface salinity (SSS); dissolved oxygen (DO); biochemical oxygen demand (BOD); and chemical oxygen demand (COD) [19]. The current estimation methods for water quality parameters primarily consist of theoretical models and empirical models. While the physical model boasts high accuracy, it necessitates a large number of parameters and presents challenges in model derivation. On the other hand, the empirical model, with its simplicity and accessibility, has emerged as the predominant approach for water quality parameter inversion. The estimation of CDOM, Chla, and TSM concentrations in rivers and lakes has mostly been conducted using Landsat 8 OLI and Sentinel-2 MSI, as demonstrated by [20,21]. However, the optical activities associated with various water quality indicators exhibit significant disparities, and the limited number of bands and band ranges in multispectral images pose challenges in capturing the more nuanced spectral information necessary to differentiate the optical activities among different water quality parameters [22]. In a related study, Wei et al. (2020) employed hyperspectral imagery to quantitatively invert the transparency of urban rivers [23].

Of these approaches, machine learning (ML) is a powerful tool that can handle complex nonlinear relationships in multiple dimensions without relying on strict statistical assumptions. As a result, ML has been extensively employed in water quality inversion studies. For instance, Li et al. (2021) utilized linear regression (LR), support vector machine (SVM), and Catboost (CB) algorithms based on multispectral images to invert the Chla concentration [24]. In a different study by Tian et al. (2023) [7], various remote sensing datasets, such as unmanned aerial vehicle (UAV) multispectral images, Sentinel-2B Multispectral Instrument (MSI) images, and Landsat 7 Enhanced Thematic Mapper Plus (ETM+) data, were utilized.

At present, there is limited research on river and estuary areas entering the sea in the Huaihe River Basin. Existing studies use satellite data with low resolution, making it difficult to undertake the high-precision monitoring of the study area. Moreover, there is a lack of a theoretical basis for the selection of inversion bands, and empirical methods are commonly used to select sensitive bands. Compared to optically active substances such as chlorophyll-a and CDOM, the spectral response of water quality parameters such as total phosphorus, ammonia nitrogen, and total nitrogen is relatively weak. In situ spectral measurements are easily influenced by optically active substances, making it challenging to directly and accurately establish the corresponding relationship between total phosphorus, ammonia nitrogen, and spectral data. Conversely, laboratory standard solution spectral measurement experiments enable the accurate analysis of the correspondence between total phosphorus, ammonia nitrogen, and spectral data, facilitating the establishment of corresponding relationships and the development of appropriate estimation models. As the model will ultimately be applied to satellite images, parameter optimization based on matching datasets from satellite and in situ observations is also necessary.

In this study, Sentinel-2 satellite remote sensing data with high spatial resolution were used. By configuring standard phosphorus and nitrogen solutions in the laboratory and collecting reflectance spectra, a correlation relationship between standard solutions and reflectance was established to find sensitive bands and establish an inversion model. The impact of different components in the water on reflectance was analyzed, and by establishing a turbidity correction coefficient, the accuracy of the inversion model was improved. By applying this model, the researchers were able to obtain information on the spatial and temporal changes in total phosphorus and ammonia nitrogen concentrations.

## 2. Data and Methods

### *2.1. Research Areas*

The downstream area of the Huaihe River Basin is located in the northern part of Jiangsu Province, China, and mainly includes rivers such as the Guanhe River, the North Jiangsu Irrigation Main Canal, the Xinyi River, and the Fanshen River. This region is densely populated, is economically developed, has a long history of agricultural cultivation, and has experienced industrial development at a rapid pace in recent years. The several rivers in the study area serve multiple functions including water supply, irrigation, and transportation. Additionally, they annually discharge a large amount of freshwater into the Yellow River, thereby significantly impacting the water quality not only in the local area but also in the seawater. This has substantial implications for both the livelihoods of the local population and the quality of seawater.

### *2.2. Data*

#### 2.2.1. Experimental Data

The National Surface Water Quality Automatic Monitoring Real-time Data Release System (https://szzdjc.cnemc.cn:8070/GJZ/Business/Publish/Main.html, from 1 January 2022 to 31 December 2022) provides data on water temperature, pH, dissolved oxygen, electrical conductivity, turbidity, permanganate index, ammonia nitrogen, total phosphorus, total nitrogen, chlorophyll-a, and algal density. This study utilized the total phosphorus and ammonia nitrogen water quality monitoring data from multiple rivers, including the Guanhe River, the North Jiangsu Irrigation Main Canal, and the Gubo Shanhoutuo River in the downstream area of the Huaihe River Basin, from January 2022 to December 2022. A total of 10 monitoring stations were selected for this study (Figure 1). Data on total phosphorus and ammonia nitrogen were provided every 4 h, resulting in a total of 20,040 sets of observed data.

#### 2.2.2. Satellite Data

This study utilized Sentinel-2 satellite data. The Sentinel-2A and Sentinel-2B satellites were successfully launched in June 2015 and March 2017, respectively. They are both equipped with a Multispectral Instrument (MSI), which has nine visible and near-infrared spectral bands. The spatial resolution ranges from 10 m for the visible and near-infrared bands to 20 m for the red edge and shortwave infrared bands. The swath width is 290 km, and the temporal resolution is 10 days [24].

Sentinel-2 satellite data can be downloaded from the Copernicus Data Hub of the European Space Agency. In this study, Sentinel-2 data from January to December 2022 were collected. Through a careful selection process, images with a high level of cloud cover were excluded, and only high-quality satellite images were chosen for water quality remote sensing inversion research.

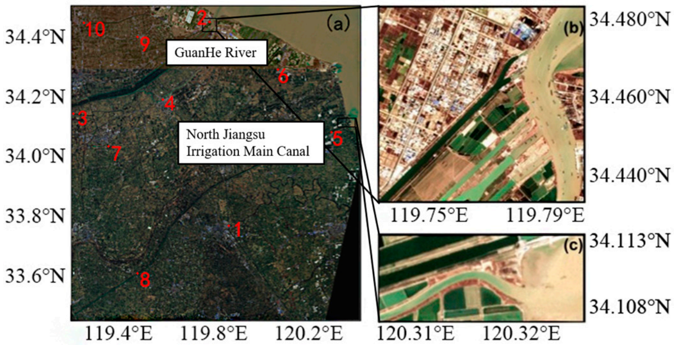


**Figure 1.** The study area: (**a**) the lower reaches of the Huaihe River Basin, (**b**) the irrigation river and the estuary area into the sea, and (**c**) the irrigation canal and the estuary area of the northern Jiangsu River. A total of 10 monitoring stations are shown in red with the site number.

*2.3. Methods*

First, the Sentinel-2 remote sensing data underwent pre-processing, including radiometric calibration, geometric correction, atmospheric correction, and land–water separation, to obtain satellite remote sensing reflectance data for the study area. Laboratory-acquired spectral reflectance data of standard solutions of total phosphorus and ammonia nitrogen were utilized to establish inversion models. The inversion models for total phosphorus and ammonia nitrogen concentration were optimized using a spatiotemporal matchup dataset that included field observations and reflected spectral data from the Sentinel-2 satellite. To enhance effectiveness, the inversion model of total phosphorus underwent tuning using turbidity-corrected data, leading to improved performance compared to the turbidity-uncorrected inversion model. This inversion model was then validated and applied to the study area to obtain the long-term distribution characteristics of total phosphorus and ammonia nitrogen concentrations. The research process of this study is shown in Figure 2.

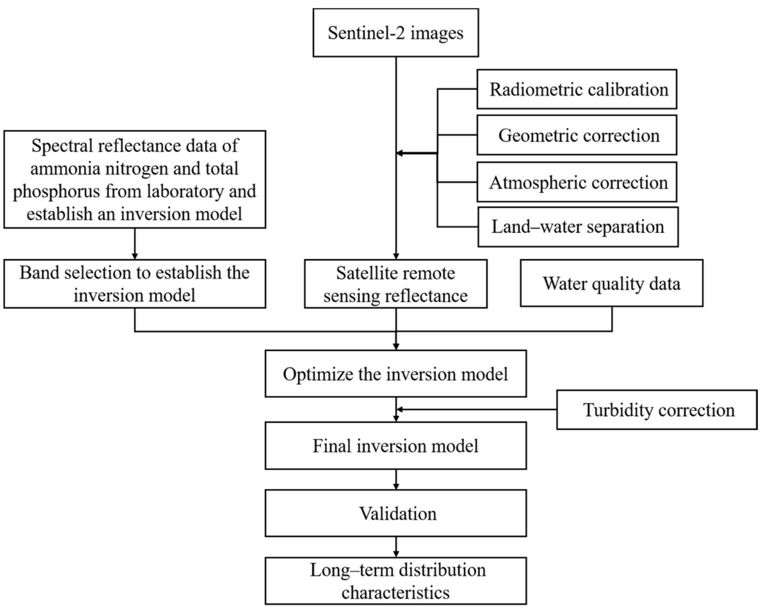


**Figure 2.** Research process.

#### 2.3.1. Laboratory Measurements

An experiment was conducted in pure water to measure the reflectance of solutions containing total phosphorus and ammonia nitrogen using sunlight as the light source. The total phosphorus concentration ranged from 0.025 to 0.375 mg/L, with 15 treatment points at intervals of 0.025 mg/L. The ammonia nitrogen concentration ranged from 0.025 to 0.4 mg/L, with 16 treatment points at intervals of 0.025 mg/L. The ASD FieldSpec Pro spectrometer (Malvern, Malvern, UK), with a wavelength range of 350 to 2500 nm and a sampling interval of 1 nm, was used for measurements.

First, a standard solution of total phosphorus was prepared by dissolving 1.532 g of pure sodium phosphate (containing 12 water molecules) in pure water and diluting it to a 1000 mL volumetric flask. After shaking well and reaching the mark, a 125 mg/L sodium phosphate standard solution (calculated as *p*) was obtained. Using a pipette, 4, 8, 12, 16, 20, 24, 28, 32, 36, 40, 44, 48, 52, 56, and 60 mL volumes of the standard solution were transferred to a 2 L black water tank to obtain samples with different concentrations for measurement.

A standard solution of ammonia nitrogen was prepared by dissolving 0.477 g of ammonium chloride in pure water and diluting it to a 1000 mL volumetric flask. After shaking well and reaching the mark, a 125 mg/L ammonium chloride standard solution was obtained. Using a pipette, 4, 8, 12, 16, 20, 24, 28, 32, 36, 40, 44, 48, 52, 56, 60, and 64 mL volumes of the standard solution were transferred to a 2 L black water tank to obtain samples with different concentrations for measurement.

When parallel light enters the interface between a sample solution and air, several processes occur: specular reflection from the water surface, absorption, scattering, and reflection by water molecules and the container, as well as absorption, scattering, and light-induced spectral signals from nitrogen and phosphorus molecules. Therefore, the spectral signal received by the spectrometer sensor should include these three components. In this study, the main focus was on the spectral signals from scattering and light-induced processes in the sample solution, while the previous two components were considered as noise, which can be represented by the mixed spectrum of water and the container. To eliminate the influence of the container and the surrounding environment on the measured data, the measured sample solution spectral data were subtracted from the mixed spectrum of water and the container, resulting in the reflectance spectrum of the sample solution.

#### 2.3.2. Pre-Processing of Satellite Data

The Sentinel-2 remote sensing data were subjected to a sequence of pre-processing procedures, encompassing radiometric calibration, geometric correction, atmospheric correction, and land–water separation. These processing steps were carried out with the specific objective of acquiring satellite remote sensing reflectance data tailored for the designated study area.

The imagery was resampled to a spatial resolution of 10 m utilizing the SNAP-ESA Sentinel Application Platformv2.0.2, with spatial resolution merging being applied across all bands to improve the signal-to-noise ratio.

We carried out atmospheric correction on the TOA reflectance data using the Image correction for atmospheric effects (iCOR) v1.0 algorithm [25], also known as OPERA v4.0 [26]. Initially, terrestrial and aquatic pixels were identified, with land pixels subsequently used to calculate the aerosol optical thickness (AOT) based on Berk et al. [27]. Subsequently, adjacency correction was performed over water using SIMEC v2.2.4 [26]. iCOR v1.0 utilizes the MODTRAN4 (MODerate resolution atmospheric TRANsmission) [28] atmospheric transmission model to simulate the impact of the atmosphere on remote sensing measurements, taking into account atmospheric constituents such as aerosols, water vapor, ozone, and optical properties. Due to the lack of multiple in situ water-leaving reflectance data, we did not conduct the precise validation of the accuracy of the above-water reflectance. However, recent studies have shown that iCOR has demonstrated good performance in atmospheric correction for Sentinel-2 imagery over inland water bodies [29,30], meeting the requirements of the inversion.

Additionally, the modified normalized difference water index (MNDWI) was utilized to differentiate between land and water. The MNDWI is a widely employed index for water body mapping [31]. This index is computed by taking the difference between the green and mid-infrared reflectance values and normalizing it using their sum.

#### 2.3.3. Inversion Model

First, based on the spectral measurements in the laboratory and the data of solution concentration, the correlation between reflectance spectra and the total phosphorus and ammonia nitrogen was analyzed. The measured laboratory spectral bands were matched with the bands of Sentinel-2 to obtain the correlation between different bands and the concentration of total phosphorus and ammonia nitrogen. Based on the correlation, bands were selected, and inversion models for total phosphorus and ammonia nitrogen were established. The bands with the highest correlation were selected, and fitting was conducted using linear, quadratic, cubic, exponential, logarithmic, and power functions to obtain single-band inversion models. Considering the subsequent transplantation of laboratory results to practical situations, combinations of sensitive bands were subjected to addition, subtraction, and division. Subsequently, modeling methods such as linear and quadratic functions were applied to build two-band inversion models for the combined bands.

Furthermore, the measured data were temporally and spatially matched with satellite data. Spatially, the pixels at the locations of observation points were selected, and temporally, a 2 h window was utilized. The data, processed according to the spatiotemporal matching criteria, formed a spatiotemporal matching dataset with the total number of 120. The dataset was randomly divided into a 7:3 ratio, with the former being used as training data for model parameter optimization and the latter (around 36) as validation data for independent validation.

Subsequently, the inversion models established in the laboratory were optimized using the training data. Due to the influence of various practical factors, single-band models were not able to achieve satisfactory results; therefore, this study primarily focused on the parameter optimization of two-band inversion models.

Additionally, it was observed during the study that the inversion model for total phosphorus was significantly affected by turbidity. Therefore, turbidity correction was applied to the total phosphorus inversion model to eliminate the effect of turbidity. In contrast to total phosphorus, ammonia nitrogen was not significantly impacted by turbidity, and thus, no turbidity correction was applied to it.

## 3. Results

### *3.1. Laboratory Measurement of Spectra and Selection of Characteristic Bands*

Due to the strong absorption of water molecules in the near-infrared range, the reflectance of nitrogen and phosphorus solutions rapidly decreases beyond the 900 nm wavelength and approaches zero. Therefore, this analysis mainly focuses on the spectral data of nitrogen and phosphorus within the wavelength range of 350 to 900 nm.

Figures 3 and 4 show that, in terms of overall reflectance, the reflectance increases significantly with the concentration of the nitrogen and phosphorus solution, showing a clear positive correlation. Phosphorus exhibits reflection peaks at 580 nm, 680 nm, 760 nm, and 820 nm. Based on the correlation coefficients between each wavelength and concentration, phosphorus shows the highest correlation at 544 nm, with a coefficient of 0.976. Overall, there are relatively high correlations across various wavelengths, with high correlations observed at 550 nm, 620 nm, and 730–780 nm in relation to the concentrations.

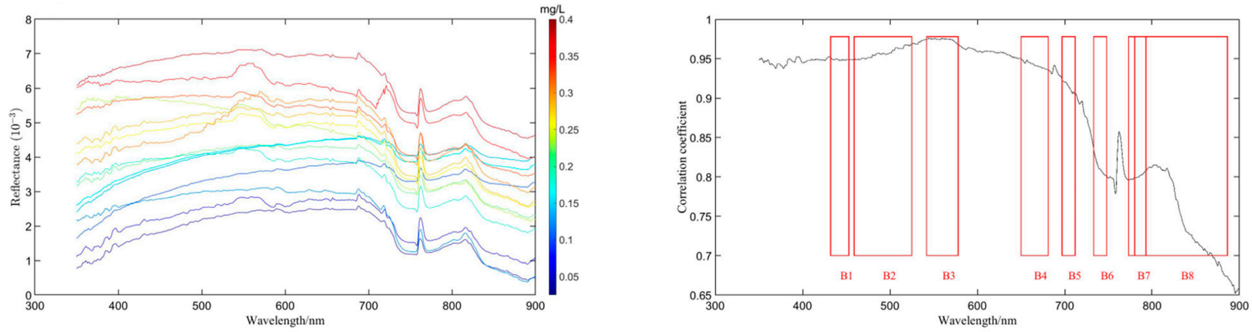


**Figure 3.** The reflectance spectra of water with different concentrations of total phosphorus solution (**left panel**) and the correlation coefficient between solution concentration and spectral bands (**right panel**). The spectral bands used by Sentinel-2 are indicated by the red boxes.

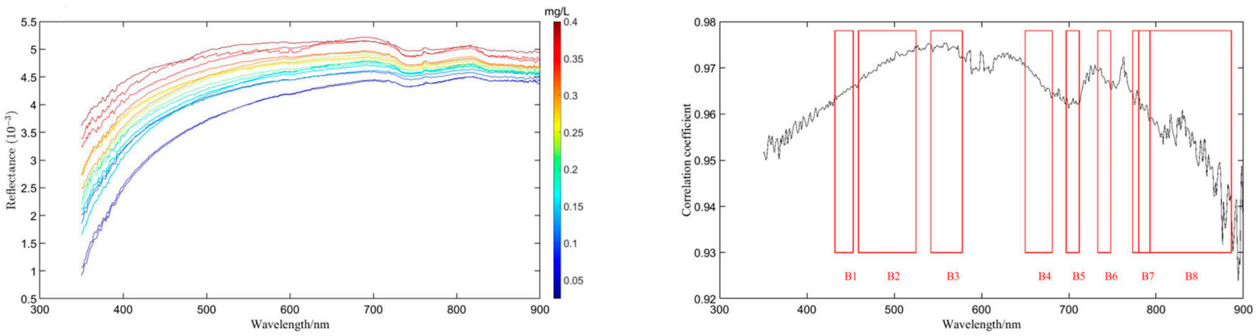


**Figure 4.** The reflectance spectra of water with different concentrations of ammonia nitrogen solution (**left panel**) and the correlation coefficient between solution concentration and spectral bands (**right panel**). The spectral bands used by Sentinel-2 are indicated by the red boxes.

### *3.2. Inversion Model for Total Phosphorus Concentration*

#### 3.2.1. Inversion Model from Laboratory Measurements

We analyzed the correlation between the total phosphorus liquid concentration and reflectance from the laboratory measurements. As shown in Figure 3, the spectral bands of Sentinel−2 exhibit a strong correlation, with the highest Pearson coefficient of 0.975 for the B3 band (Table 1).

**Table 1.** Correlation coefficient of measured reflectance to TP concentration configured in the laboratory.

| | **B1** | **B2** | **B3** | **B4** | **B5** | **B6** | **B7** | **B8** |
|---|---|---|---|---|---|---|---|---|
| TP | 0.948 | 0.957 | 0.975 | 0.942 | 0.915 | 0.810 | 0.799 | 0.750 |

When establishing inversion models, we selected four highly correlated bands, B3, B4, B5, and B6, and generated a total of 24 new combinations by performing the addition, subtraction, and division of any two sensitive bands. These combinations were then subjected to correlation analysis, and the band combination of $B5/B3$ was utilized to establish a model for TP concentration inversion. By employing the linear fitting, polynomial fitting, exponential fitting, and power function fitting methods, the inversion model for total phosphorus concentration in the laboratory's ideal environment was obtained, as shown in Table 2.

**Table 2.** Comparison of TP concentration inversion models for different forms of laboratory measurements.

| Algorithms | $R^2$ | RMSE |
|---|---|---|
| $TP = -0.8788 \times (B5/B3) + 1.024$ | 0.8316 | 0.08117 |
| $TP = -1.054 \times (B5/B3)^2 + 1.11 \times (B5/B3) + 0.09473$ | 0.8374 | 0.08714 |
| $TP = 165.9 \times (B5/B3)^3 - 466.7 \times (B5/B3)^2 + 434.3 \times (B5/B3) - 133.4$ | 0.8359 | 0.05684 |
| $TP = 7.941 \times e^{3.975\times(B5/B3)}$ | 0.7865 | 0.08499 |
| $TP = -0.8172ln(B5/B3) + 0.1442$ | 0.8240 | 0.08183 |
| $TP = 0.151 \times (B5/B3)^{-3.524}$ | 0.7674 | 0.08656 |

The model that yielded favorable results for total phosphorus concentration retrieval is as follows:

$$TP = 165.9 \times (B5/B3)^3 - 466.7 \times (B5/B3)^2 + 434.3 \times (B5/B3) - 133.4 \quad (1)$$

The determination coefficient $R^2$ for the model is 0.8359, and the root mean square error is 0.05684.

#### 3.2.2. Inversion Model Optimized Using Matchup Datasets

Applying the model to Sentinel-2 remote sensing reflectance data and validating it with actual measurements shows that the relative errors at each measurement point are all greater than 50%. This indicates that the model cannot be directly applied to satellite remote sensing reflectance data and requires optimization. Next, the Sentinel-2 remote sensing reflectance data matched in space and time were used, along with actual total phosphorus concentration data, to establish the model.

Based on the correlation between total phosphorus concentration and the various spectral bands, the correlation coefficients of the B3, B4, B5, and B6 bands all exceed 0.6. The experimental findings indicate a higher correlation of the phosphorus solution within the 550 nm to 750 nm range, which aligns well with the four bands of B3, B4, B5, and B6.

Of the aforementioned four sensitive bands, a total of 24 different combinations were obtained by adding, subtracting, or calculating the ratio of any two sensitive bands. The best-performing band combinations in terms of correlation were identified as $B3$–$B5$ and $B5/B3$, and these two combinations were selected for the retrieval of total phosphorus concentration.

Using reflectance as the independent variable and total phosphorus concentration as the dependent variable, data were fitted using linear, quadratic, cubic, exponential, logarithmic, and power functions, as detailed in Table 3.

**Table 3.** Comparison of TP concentration inversion models based on matching data in different forms.

| Algorithms | $R^2$ | RMSE |
|---|---|---|
| $TP = -0.9315 \times (B3 - B5) + 0.1099$ | 0.6621 | 0.0223 |
| $TP = 3.059 \times (B3 - B5)^2 - 0.9061 \times (B3 - B5) + 0.1054$ | 0.6713 | 0.02282 |
| $TP = -168.2 \times (B3 - B5)^3 + 5.105 \times (B3 - B5)^2 - 0.4095 \times (B3 - B5) + 0.09616$ | 0.6827 | 0.02334 |
| $TP = 0.104 \times e^{-8.358\times(B3-B5)}$ | 0.6725 | 0.02195 |
| $TP = 0.2101 \times (B5/B3) - 0.09688$ | 0.6345 | 0.02319 |
| $TP = 0.2463 \times (B5/B3)^2 - 0.2585 \times (B5/B3) + 0.1165$ | 0.6955 | 0.02156 |
| $TP = -0.6444 \times (B5/B3)^3 + 2.068 \times (B5/B3)^2 - 1.954 \times (B5/B3) + 0.6408$ | 0.6543 | 0.02436 |
| $TP = 0.1973ln(B5/B3) + 0.1151$ | 0.6099 | 0.02396 |
| $TP = 0.01506 \times e^{1.969\times(B5/B3)}$ | 0.6528 | 0.02216 |
| $TP = 0.111 \times (B5/B3)^{1.972}$ | 0.6481 | 0.02276 |

The following model yielded favorable results for total phosphorus concentration retrieval:

$$TP = 0.2463 \times (B5/B3)^2 - 0.2585 \times (B5/B3) + 0.1165 \quad (2)$$

The determination coefficient ($R^2$) for the model is 0.6955, and the root mean square error (RMSE) is 0.02156 mg/L.

When using the independent data ($n$ = 36) to validate the model, the determination coefficient $R^2$ for the model is 0.6556, and the root mean square error is 0.02367 mg/L. The results at certain points are shown in Table 4, including the total phosphorus concentration, the retrieval results, the absolute error of the retrieval results, and the relative error.

**Table 4.** Validations of TP concentration inversion model.

| | Measured TP | Retrievals | Absolute Errors | Relative Errors |
|---|---|---|---|---|
| 1 | 0.1878 | 0.1651 | 0.0227 | 12.08% |
| 2 | 0.0861 | 0.0999 | 0.0138 | 16.11% |
| 3 | 0.139 | 0.1647 | 0.0257 | 18.47% |
| 4 | 0.094 | 0.0823 | 0.0117 | 12.44% |
| 5 | 0.1182 | 0.0879 | 0.0303 | 25.61% |

3.2.3. Turbidity Correction

In order to address the insufficient performance of the model, we analyzed the impact of water composition in the inversion results. The results reveal that turbidity has a significant impact on the retrieval model. Turbidity correction was conducted for the TP inversion model.

Firstly, a linear model between turbidity and each spectral band is established, with the coefficient of turbidity as the turbidity correction factor. This factor is used to eliminate the influence of turbidity on the dependent variable, reflectance. Next, the reflectance data are adjusted using the correction factor, resulting in turbidity-corrected reflectance data. The turbidity-corrected reflectance data for each band are denoted as $B1_{TC}$, $B2_{TC}$, $B3_{TC}$, $B4_{TC}$, $B5_{TC}$, $B6_{TC}$, $B7_{TC}$, and $B8_{TC}$. These adjusted data are then applied to the retrieval of water quality parameter concentrations.

The model for the retrieval of total phosphorus concentration after turbidity correction is as follows:

$$\begin{aligned} TP = {} & 1.094 \times 10^{-9} \times (B5_{TC} + B8_{TC})^3 - 2.878 \times 10^{-6} \times (B5_{TC} + B8_{TC})^2 \\ & + 0.002509 \times (B5_{TC} + B8_{TC}) - 0.616 \end{aligned} \quad (3)$$

The coefficient of determination is 0.7812, and the root mean square error is 0.0219 mg/L after turbidity correction. This indicates a significant improvement compared to the pre-correction model, where the $R^2$ was 0.6955.

The same independent data ($n$ = 36) were applied to validate the turbidity-correction model with $R^2$ = 0.7302 and RMSE = 0.02614 mg/L. Comparisons of results between the models with and without turbidity correction are shown in Table 5 for specific points. It can be observed that turbidity correction resulted in significant improvements.

**Table 5.** Verification results of TP concentration inversion model (TC: turbidity correction).

| | Measured TP | Results before TC | Relative Errors | Results after TC | Relative Errors |
|---|---|---|---|---|---|
| 1 | 0.1878 | 0.1651 | 12.08% | 0.1946 | 3.64% |
| 2 | 0.0861 | 0.0999 | 16.11% | 0.0878 | 2.02% |
| 3 | 0.139 | 0.1647 | 18.47% | 0.1608 | 15.68% |
| 4 | 0.094 | 0.0823 | 12.44% | 0.097 | 3.23% |
| 5 | 0.1182 | 0.0879 | 25.61% | 0.1351 | 14.31% |

### 3.3. Inversion Model for Ammonia Nitrogen Concentration

Using the same method, through the comparison of various results obtained via band combination and polynomial fitting, the optimal estimation model for ammonia nitrogen concentration under ideal experimental conditions was selected as follows:

$$NH_3 - N = 3.333 \times (B7/B1)^2 - 9.328 \times (B7/B1) + 6.56 \quad (4)$$

The determination coefficient $R^2$ for the model is 0.9036, and the root mean square error is 0.03969 mg/L.

The model was subsequently optimized using the matchup dataset. Using reflectance as the independent variable and ammonia nitrogen concentration as the dependent variable, data were fitted using linear, quadratic, cubic, exponential, logarithmic, and power functions, as detailed in Table 6.

$$NH_3 - N = -2.633 \times (B7/B1)^3 + 9.269 \times (B7/B1)^2 - 10.16 \times (B7/B1) + 3.64 \quad (5)$$

**Table 6.** Comparison of different forms of ammonia nitrogen inversion models.

| Algorithms | $R^2$ | RMSE |
|---|---|---|
| $NH_3 - N = 0.1226 \times e^{-10.17 \times (B1-B7)}$ | 0.7853 | 0.0465 |
| $NH_3 - N = -1.894 \times (B1 - B7) + 0.1427$ | 0.7476 | 0.05042 |
| $NH_3 - N = 13.45 \times (B1 - B7)^2 - 1.012 \times (B1 - B7) + 0.1103$ | 0.8106 | 0.04545 |
| $NH_3 - N = 285.8 \times (B1 - B7)^3 + 32.53 \times (B1 - B7)^2 -2.156 \times (B1 - B7) + 0.1134$ | 0.883 | 0.03732 |
| $NH_3 - N = -2.059 \times (B2 - B7) + 0.1719$ | 0.8143 | 0.04325 |
| $NH_3 - N = 17.11 \times (B2 - B7)^2 - 1.564 \times (B2 - B7) + 0.1247$ | 0.8731 | 0.03721 |
| $NH_3 - N = -61.03 \times (B2 - B7)^3 + 16.34 \times (B2 - B7)^2 -1.303 \times (B2 - B7) + 0.1205$ | 0.8736 | 0.03879 |
| $NH_3 - N = 0.1409 \times e^{-11.6 \times (B2-B7)}$ | 0.8635 | 0.03708 |
| $NH_3 - N = 0.375 \times (B7/B1) - 0.2252$ | 0.7344 | 0.05171 |
| $NH_3 - N = 0.6457 \times (B7/B1)^2 - 1.097 \times (B7/B1) + 0.5583$ | 0.8227 | 0.04398 |
| $NH_3 - N = -2.633 \times (B7/B1)^3 + 9.269 \times (B7/B1)^2 -10.16 \times (B7/B1) + 3.64$ | 0.8997 | 0.03454 |
| $NH_3 - N = 0.1339 \times (B7/B1)^{2.421}$ | 0.7837 | 0.04667 |
| $NH_3 - N = 0.3932 \times ln(B7/B1) + 0.1599$ | 0.6717 | 0.0575 |
| $NH_3 - N = 0.01607 \times e^{2.067 \times (B7/B1)}$ | 0.7877 | 0.04624 |

The determination coefficient $R^2$ for the model is 0.8997, and the root mean square error is 0.03454 mg/L.

The independent data ($n$ = 36) were used to analyze the retrieval results of the model. The determination coefficient $R^2$ for the model is 0.8024, and the root mean square error is 0.0368 mg/L. The results for certain points are shown in Table 7, including the ammonia nitrogen concentration, the retrieval results, the absolute error of the retrieval results, and the relative errors.

**Table 7.** Validations of the ammonia nitrogen concentration inversion model.

| | Measured $NH_3$-N | Retrievals | Absolute Errors | Relative Errors |
|---|---|---|---|---|
| 1 | 0.3547 | 0.3594 | 0.0047 | 1.33% |
| 2 | 0.0849 | 0.0880 | 0.0031 | 3.69% |
| 3 | 0.3501 | 0.3472 | 0.0030 | −0.84% |
| 4 | 0.1005 | 0.0853 | 0.0152 | −15.11% |
| 5 | 0.0769 | 0.0857 | 0.0088 | 11.49% |

*3.4. Temporal and Spatial Variation Characteristics of Total Phosphorus and Ammonia Nitrogen*

The inversion models were validated using independent data, demonstrating their good performance. Subsequently, these models were applied to the irrigation area of the Guanhe River, the lower reaches of the North Jiangsu Irrigation Main Canal, and the estuarine area, resulting in concentration distribution maps of total phosphorus and ammonia nitrogen in the water bodies of this region. Figures 5 and 6, respectively, depict the distributions of ammonia nitrogen and total phosphorus concentrations in the Guanhe River's coastal area in 2022. Similarly, Figures 7 and 8, respectively, show the distributions of ammonia nitrogen and total phosphorus concentrations in the North Jiangsu Irrigation Main Canal area in 2022.

Based on Figures 5 and 6, the ammonia nitrogen concentration in the Guanhe River and the estuarine area ranges from approximately 0.05 to 0.25 mg/L, while the total phosphorus concentration ranges from approximately 0.1 to 0.4 mg/L. These two water quality parameters exhibit slightly higher concentrations in the southern part of the estuarine area compared to the northern part. However, within the annual range, the ammonia nitrogen concentration in the southern area remains relatively stable, while the northern area shows a higher correlation with the river flow. This may be attributed to the southern and northern areas of the estuary being separated by embankments, resulting in less influence from the diluting water of the Guanhe River in the southern region. The concentrations in the South Pianhong, North Pianhong, and Xinyi Rivers, which discharge into the Guanhe River, are lower compared to the Guanhe River itself, leading to the formation of low-concentration zones in the areas where they merge.

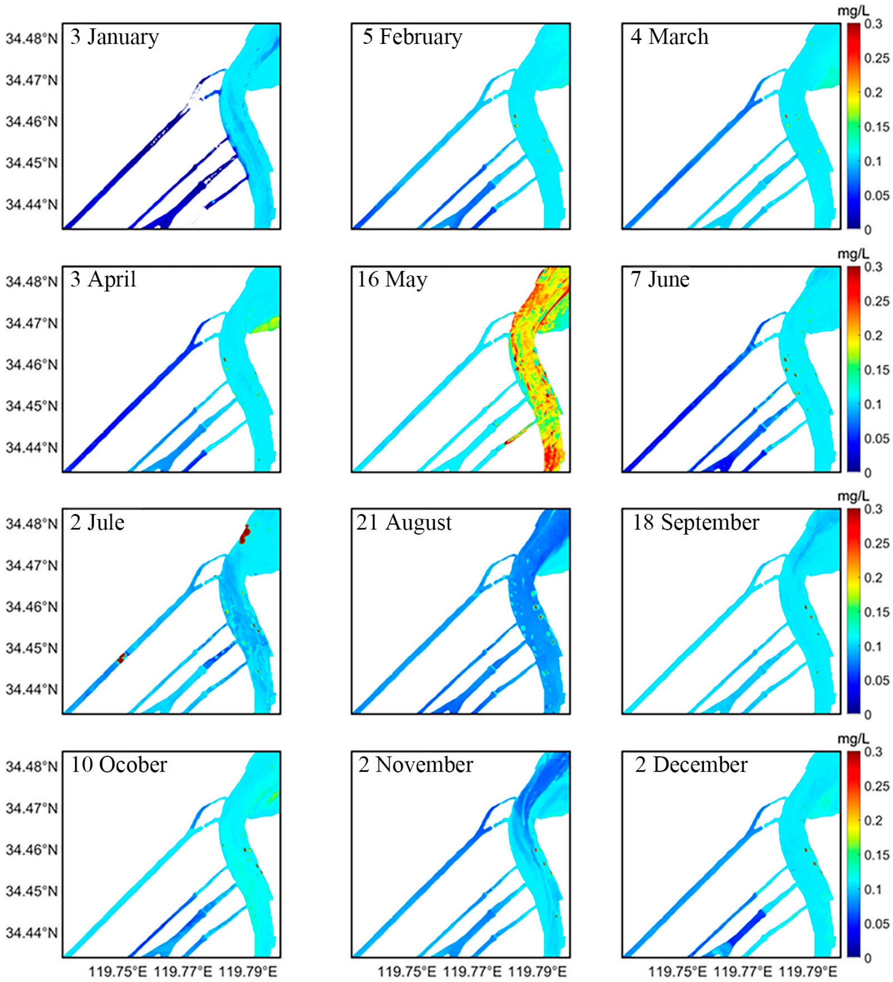


**Figure 5.** Distribution of ammonia nitrogen concentration in the area of the Guanhe flowing into the sea in 2022.

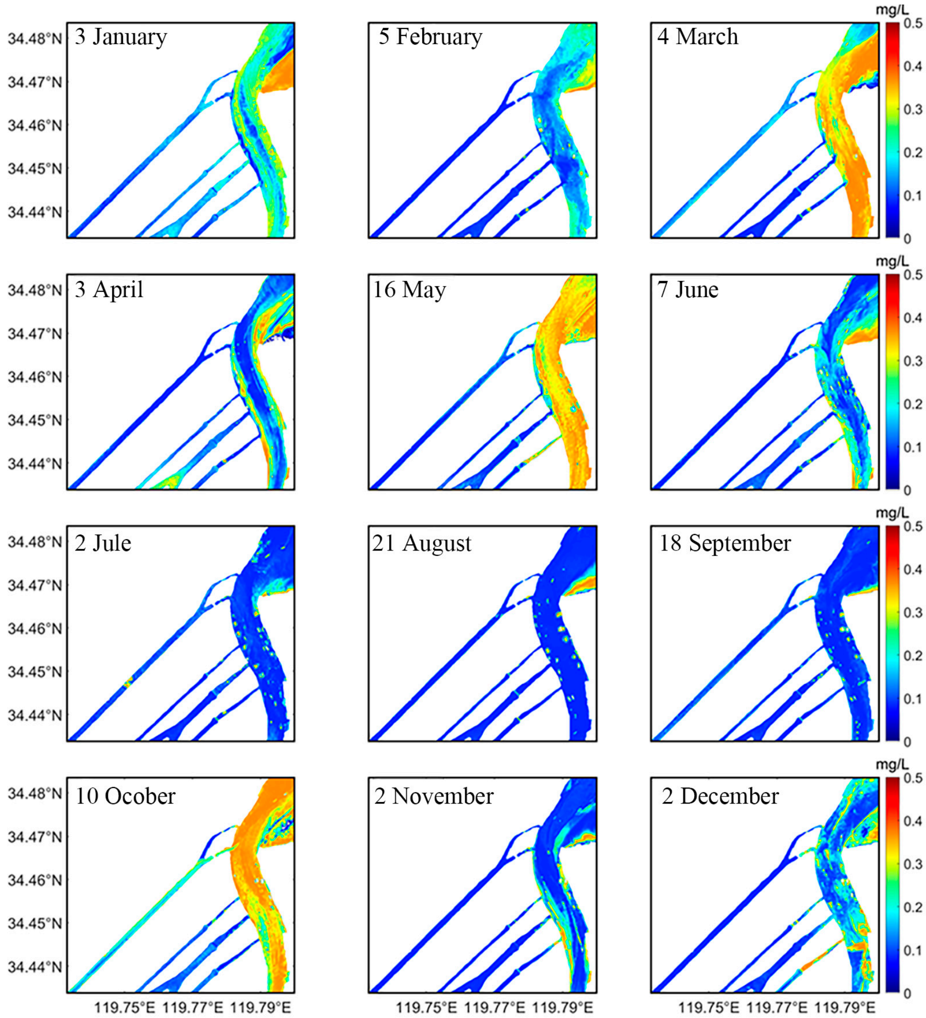


**Figure 6.** Distribution of TP concentration in the area of Guanhe flowing into the sea in 2022.

Throughout the year, there are high correlations between the variations in total phosphorus and ammonia nitrogen concentrations. The majority of the areas show low concentrations of ammonia nitrogen, mostly below 0.15 mg/L, and low concentrations of total phosphorus, mostly below 0.25 mg/L. On 16 May, both the total phosphorus and ammonia nitrogen exhibited high concentrations. According to the data from the real-time monitoring system for national surface water quality, the water quality on that day was poor, with the water quality category at the Yanwei Gate Water Quality Monitoring Station being Class IV. On 4 March and 10 October, the total phosphorus concentrations were relatively high, with the water quality category at the Yanwei Gate Water Quality Monitoring Station being Class III.

In Figure 7, the total phosphorus concentration in the Northern Jiangsu irrigation canal and the estuarine area ranges from approximately 0.1 to 0.4 mg/L. The total phosphorus exhibits stable concentrations within the Northern Jiangsu irrigation canal, with minimal variations throughout the year. Due to the limited inflow of tributaries, the water in the Northern Jiangsu irrigation canal remains stable. During the period of remote sensing image acquisition, this region experienced minimal precipitation, leading to the slight variation in total phosphorus concentration. In the marine environment, the total phosphorus concentration is relatively higher, influenced by the dilution of river water, resulting in lower concentrations in the estuarine area. On 3 January 2022, the total phosphorus concentration in the Northern Jiangsu irrigation canal was low, and from February to April, it remained relatively stable. On 16 May, the total phosphorus concentration in the canal exhibited minimal variation, but a higher concentration was observed near the coastal area, influenced by the inflow of river water, leading to lower concentrations in the estuarine area. Minimal variation in total phosphorus concentration was observed in June, July, September, October, November, and December. On 21 August, the total phosphorus concentration in the canal was low.

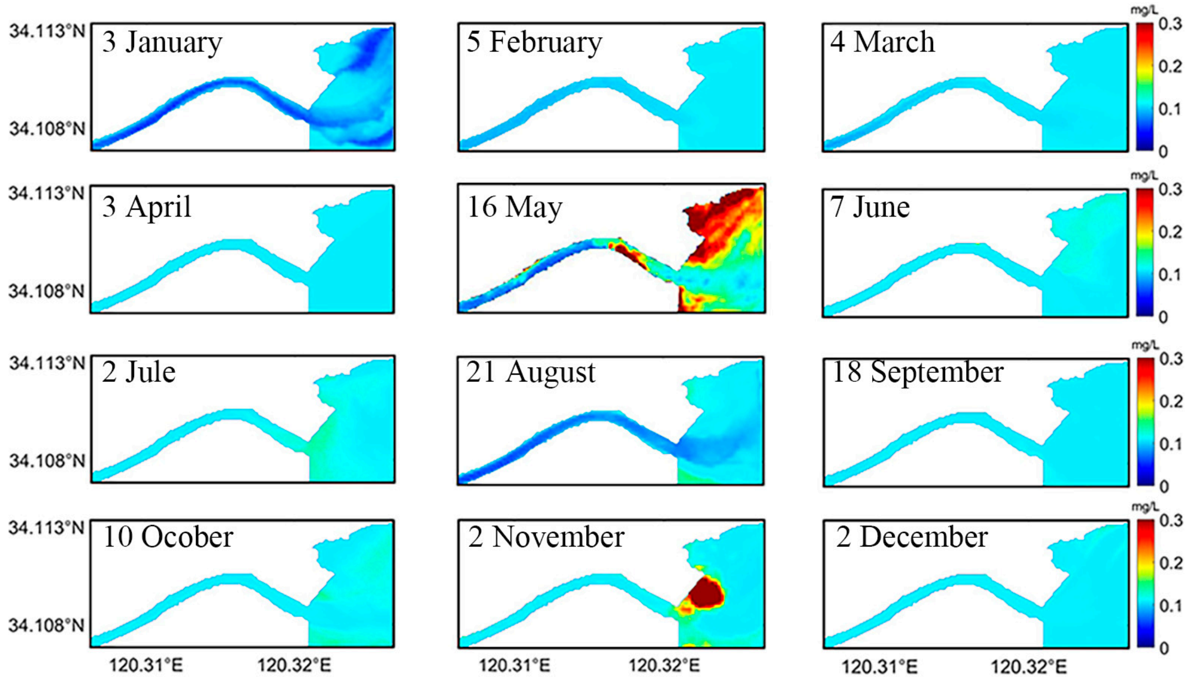


**Figure 7.** Distribution of TP concentration in the area of the main irrigation canal in northern Jiangsu in 2022.

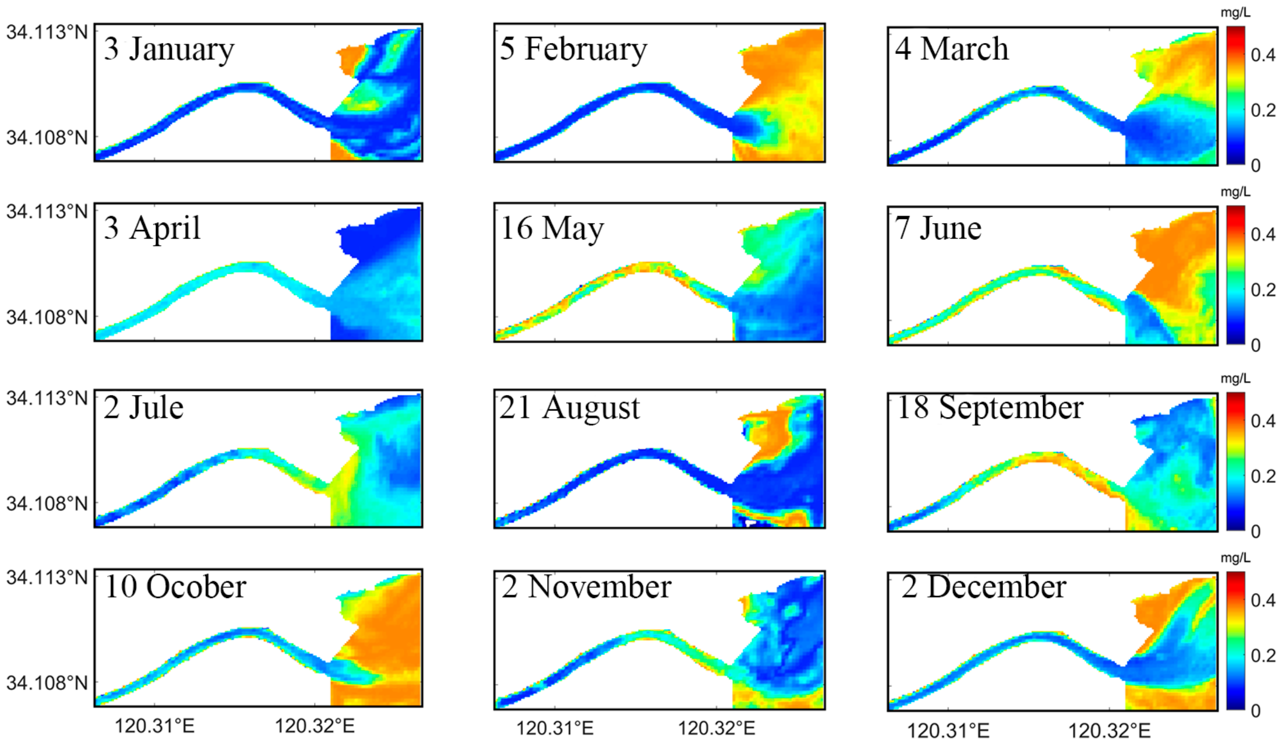


**Figure 8.** Distribution map of ammonia nitrogen concentration in the sea area of the main irrigation canal in northern Jiangsu in 2022.

As shown in Figure 8, the ammonia nitrogen concentration in the Northern Jiangsu irrigation canal and the estuarine area ranges from approximately 0.05 to 0.3 mg/L, demonstrating greater variations in patterns compared to total phosphorus. In January, February, and March, the ammonia nitrogen concentration in the river area of the Northern Jiangsu irrigation canal was low, with a concentration range of approximately 0.05–0.15 mg/L. From April to June, the ammonia nitrogen concentration in the river area gradually increased, with a higher concentration observed on May 16, indicating poor water quality as per the real-time data from the National Surface Water Quality Automatic Monitoring System. In July and August, the ammonia nitrogen concentration gradually decreased, reaching approximately 0.1 mg/L on 21 August. In September, October, and November, the ammonia nitrogen concentration in the river area of the Northern Jiangsu irrigation canal was relatively high, with a range of approximately 0.2–0.3 mg/L. On 2 December, the ammonia nitrogen concentration decreased. In the estuarine and nearshore areas, the ammonia nitrogen concentration was relatively high, influenced by the dilution of river water. In January, February, March, June, August, October, November, and December, lower ammonia nitrogen concentrations were observed in the estuarine area. From April to September, higher ammonia nitrogen concentrations were observed in the river area of the Northern Jiangsu irrigation canal compared to the nearshore area, indicating the formation of a high-ammonia-nitrogen-concentration zone in the nearshore due to the inflow of river-borne ammonia nitrogen.

## 4. Discussion

In this study, laboratory-measured models have shown that single-band models can achieve good results. As shown in Table 8, using $B3$-band reflectance data can effectively invert the concentrations of total phosphorus and ammonia nitrogen.

**Table 8.** Comparison of single band TP concentration inversion models with different forms.

| Algorithms | $R^2$ | RMSE |
|---|---|---|
| $TP = 78.65 \times B3 - 0.1698$ | 0.9514 | 0.02558 |
| $TP = -592.5 \times B3^2 + 84.25 \times B3 - 0.182$ | 0.9515 | 0.02659 |
| $TP = -3.54 \times 10^6 \times B3^3 + 5.028 \times 10^4 \times B3^2 - 146.1 \times B3 + 0.1432$ | 0.9574 | 0.02605 |
| $TP = 0.03561 \times e^{347.5 \times B3}$ | 0.8831 | 0.03966 |
| $TP = 0.3413 ln(B3) + 2.045$ | 0.9277 | 0.03119 |
| $TP = 3499 \times (B3)^{1.832}$ | 0.9329 | 0.03006 |

The following model yielded favorable results for total phosphorus concentration retrieval:

$$TP = -3.54 \times 10^6 \times B3^3 + 5.028 \times 10^4 \times B3^2 - 146.1 \times B3 + 0.1432 \tag{6}$$

The determination coefficient $R^2$ for the model is 0.9574, and the root mean square error is 0.02605.

However, when applying the models to the study area, it is necessary to fully consider the differences between laboratory measurements and actual conditions. In real water bodies, chlorophyll-a, CDOM, and particulate matter serve as the primary influencing factors on water spectral properties. Field-measured spectra are simultaneously influenced by multiple water components and cannot be singularly correlated with total phosphorus or ammonia nitrogen concentrations as in laboratory measurements. During the research process, it was found that directly calibrating the single-band model with the matching data from field measurements and Sentinel-2 did not yield favorable results due to the low correlation of the single band in the matching dataset. Therefore, for total phosphorus, we selected four highly correlated bands, B3, B4, B5, and B6, and generated a total of 24 new combinations by performing the addition, subtraction, and division of any two sensitive bands. These combinations were then subjected to correlation analysis, and the highly correlated band combinations were selected to establish the model.

Starting from the perspective of laboratory experiments, this study used the method of standard solution preparation combined with spectral measurements to obtain data and establish models for band selection. This approach effectively elucidates the relationship between water quality parameters and spectral responses in different bands, and the constructed models accurately reflect the spectral impact of water quality parameters. However, when applying the ideal experimental model to satellite remote sensing, it is essential to consider that the spectra received by satellites actually contain complex water optical components, necessitating a thorough model calibration. In this study, a spatiotemporal matchup dataset was constructed using water quality parameters and Sentinel-2 spectral data measured throughout the year 2022. This dataset was utilized for the parameter calibration and model optimization of the ideal experimental model, yielding satisfactory results. Nevertheless, the lack of matched field-measured water reflectance spectra hinders the direct analysis of differences between laboratory-measured spectra and field-measured water spectra. This is an important aspect, and the next step will involve conducting simultaneous field water spectral measurement experiments to analyze the differences between field-measured spectra and laboratory-measured spectra; evaluate the influence of optical active substances such as chlorophyll-a, CDOM, and particulate matter; and facilitate the better analysis of the selection of band combinations and improved model optimization.

The inversion model established in this study for ammonia nitrogen and total phosphorus concentrations is based on the long-term and wide-ranging spatiotemporal matching of in situ measurements and remote sensing reflectance data. After model establishment, we conducted an analysis of the influence of different water constituents in the model, such as chlorophyll-a, CDOM, and turbidity. The study revealed that chlorophyll-a and CDOM have minimal impacts on total phosphorus and ammonia nitrogen. This finding is reasonable considering that total phosphorus and ammonia nitrogen are not primarily present in chlorophyll-a and CDOM, and the spectral bands used for the inversion of total phosphorus and ammonia nitrogen are not sensitive to chlorophyll-a or CDOM. However, turbidity has a significant impact on total phosphorus. Based on the dataset used in this study, correcting for turbidity in the inversion model for total phosphorus significantly improves the inversion accuracy. As shown in Table 5, the inversion results for each validation site are improved to varying degrees. Similarly, applying turbidity correction to ammonia nitrogen did not yield the same positive results (Table 9). This could be attributed to the fact that total phosphorus includes particulate components, while ammonia nitrogen is present primarily in a dissolved state. Consequently, changes in turbidity have a more significant effect on total phosphorus, whereas the impact on ammonia nitrogen is less apparent. For the inversion of total phosphorus concentration, a turbidity correction method is employed to reduce the impact of differences in water turbidity on the accuracy of the model. However, turbidity correction is not applied to ammonia nitrogen.

**Table 9.** Validations of ammonia nitrogen concentration inversion model (TC: turbidity correction).

| | **Measure $NH_3$-N** | **Results before TC** | **Relative Errors** | **Results after TC** | **Relative Errors** |
|---|---|---|---|---|---|
| 1 | 0.3547 | 0.3594 | 1.33% | 0.3604 | 1.61% |
| 2 | 0.0849 | 0.0880 | 3.69% | 0.0800 | 5.73% |
| 3 | 0.3501 | 0.3472 | −0.84% | 0.3322 | 5.13% |
| 4 | 0.1005 | 0.0853 | −15.11% | 0.0847 | −15.69% |
| 5 | 0.0769 | 0.0857 | 11.49% | 0.0849 | 10.34% |

After the establishment of the model, we validated the model using a matched independent testing dataset. The correlation of the total phosphorus inversion model was 0.7302, with a root mean square error of 0.02614 mg/L, and the correlation for ammonia nitrogen was 0.8024, with a root mean square error of 0.0568 mg/L. The model achieved good performance. To gain a better understanding of the inversion performance of the model, we compared the results of this study with previous research. In Tables 10 and 11, the mean relative error (MRE), mean absolute percentage error (MAPE), $R^2$, and RMSE are taken as the evaluation metrics to evaluate the inversion performance of the model.

**Table 10.** Comparisons of the model performance of the total phosphorus inversion models.

| Author | Inverse Model | Study Area | Sensor | Error |
|---|---|---|---|---|
| Xiong et al. [32] | TP = 0.2553 × ($B2$ − $B5$)/($B2$ + $B5$) −0.0084 | Lake Hongze | MODIS | $R^2$ = 0.607, RMSE = 0.031 mg/L, MRE = 37.584% |
| Li et al. [33] | TP = 0.1965 × $R$(740)/$R$(670)) + 0.027 | Lake Taihu, Fuchunjiang Reservoir, and Liangxi River | GHPS | $R^2$ = 0.85, MAPE= 15.0% |
| Shang et al. [34] | TP = −5.3248 × ln($B4$)/$B4$ + 0.0885 | Poyang lake | Landsat 8 | $R^2$ = 0.7589, RMSE = 0.0048 mg/L |
| Wu et al. [35] | Ln(TP) = −21.45($B3$/$B2$) − 14.42($B1$/$B3$) +42.99($B1$) + 27.1 | Qiantang River | Landsat TM | $R^2$ = 0.77, RMSE = 0.77 mg/L |
| Du et al. [36] | TP= −6.739 × ($B_{488}$ − $B_{670}$) −0.217 × ($B_{670}$ − $B_{865}$)/($B_{670}$ + $B_{865}$) + 0.303; | Lake Taihu | GOCI | $R^2$ = 0.898 MAE = 33.642% |
| Liu et al. [37] | TP = −15.51 × $B3$+ 2.81 | Lake Cihu | IKONOS | $R^2$ = 0.84, RMSE = 0.17 mg/L |
| Cruz-Retana et al. [38] | LogTP = 1.3544 + 0.1240 × ($B5$/$B4$) + 0.04610($B5$/$B6$) | A water body in the Mexican highlands | Landsat 8 OLI | $R^2$ = 0.79, RMSE = 9.63 mg/L |
| Zhao et al. [39] | TP = −33.64$X^3$ + 19.39$X^2$ − 1.79$X$ + 0.08766, $X$= 1 − 3($B7$ + $B8$A + $B11$) [min($B7$, $B8A$, $B11$)] | Yangtze River | Sentinel-2A | $R^2$ = 0.74, RMSE = 0.07 mg/L |

**Table 11.** Comparisons of the model performance of the ammonia nitrogen inversion models.

| Author | Inverse Model | Study Area | Sensor | Error |
|---|---|---|---|---|
| Dong et al. [40] | $NH_3$-N = 0.474 × $B_{550}$/$B_{488}$ + 0.276; | Danjiangkou Reservoir | Sentinel-2 | $R^2$ = 0.739, RMSE = 0.0107 mg/L |
| He et al. [41] | ln($NH_3$-N) = −7.177 + 1.93ln($B7$) + 0.1323($B6$) −2.185($B6$/$B3$)−0.07648$B1$ | Guanting Reservoir | Landsat 5 TM | $R^2$ = 0.806, MRE = 28% |
| Ma et al. [42] | $NH_3$-N =1.7313(($B3$ + $B4$)/$B1$) − 3.9968 | Tangxun lake | GF-2, GF-6 | $R^2$ = 0.8497, MRE = 21.53% |
| Wu et al. [43] | $NH_3$-N =0.219 + 0.001($B5$ + $B7$) | Haihe River | Landsat 8 OLI | $R^2$ = 0.611, MAD = 0.404 |
| Al-Shaibah et al. [44] | $NH_3$-N= 0.8 × ($B_{red}$ + $B_{NIR}$) + ($B_{blue}$/$B_{NIR}$) × ($B_{blue}$ + $B_{NIR}$)+ ($B_{blue}$/$B_{NIR}$) × 0.099 | Erlong Lake | Landsat TM5, ETM7, and OLI8 | $R^2$ = 0.862, RMSE = 0.645 mg/L |

From the comparison in Table 10, it can be observed that the $R^2$ values for total phosphorus range from 0.60 to 0.89, while the RMSE values mostly fall between 0.0048 and 0.17 mg/L. The accuracy of the results in this study is comparable to that in previous studies, with smaller RMSE values compared to those obtained by other researchers, except for the values that were larger when compared to Shang's results [34].

Similarly, from the comparison in Table 11 for ammonia nitrogen, it can be seen that the findings in this study are consistent with previous research. In other studies, the $R^2$ values range from 0.61 to 0.86, while the RMSE values mostly fall between 0.01 mg/L and 0.64 mg/L.

The above comparisons indicated that the models can effectively invert the concentrations of ammonia nitrogen and total phosphorus in the study area, facilitating the large-scale and long-term monitoring of these concentrations. Moreover, they provide a reference for analyzing the distribution characteristics of nutrients and understanding water pollution conditions. However, the inversion model established in this study requires substantial support from in situ measurements, and it imposes high demands on input data. The collection of data for extreme conditions may be incomplete, leading to potential shortcomings in the model's response to such extreme situations. Thus, it is necessary to continue increasing the number of in situ data samples.

Unlike in the present research, there were few previous studies that employed remote sensing methods for monitoring the study area, thus prohibiting direct comparative analysis. A thorough investigation has been conducted on the long-term trends and potential sources of water quality parameters within the study area [3,45]. Chen et al. conducted an analysis of water quality changes in the Huaihe River Basin, utilizing data from 110 monitoring sections spanning the period of 2003 to 2019 [3]. The results indicated an increasing trend in TP within the downstream area, while ammonia nitrogen exhibited a clear decreasing trend. This study did not observe any increasing trends in annual TP variations, as TP consistently maintained a relatively low state throughout the year. In their analysis of irrigation canals, Tian et al. studied the characteristics of variations in water quality parameters and their driving factors [45]. Both total phosphorus and ammonia nitrogen pollution sources were predominantly associated with agricultural pollution.

According to Figures 5 and 6, the inversion results indicate the occurrence of high concentrations of total phosphorus and ammonia nitrogen in the estuarine areas of the Guanhe River and the North Jiangsu Irrigation Main Canal on 16 May. According to data from the real-time monitoring system for national surface water quality, the water quality on that day was poor, with the water quality category at the Yanwei Gate Water Quality Monitoring Station being Class IV. According to the agricultural departments in Lianyungang and Yancheng, rice planting generally begins from April to May, while corn is a summer crop typically sown from May to June. During this period, a large amount of nitrogen and phosphorus fertilizer is applied as base fertilizer, possibly resulting in the inflow of pollutants from farmland and agricultural drainage into rivers and estuaries, leading to high concentrations of total phosphorus and ammonia nitrogen in the water. The inversion results also indicate the occurrence of high total phosphorus concentrations in the estuarine areas of the Guanhe River and the North Jiangsu Irrigation Main Canal on 10 October. According to the agricultural departments in Lianyungang and Yancheng, wheat is a winter crop usually sown from October to November, and phosphorus fertilizer is an important fertilizer for promoting root development and flower bud differentiation, which is typically applied in the early growth stage of wheat. This practice may result in the discharge of agricultural wastewater into rivers, leading to water pollution.

According to Figures 7 and 8, the ammonia nitrogen concentration in the North Jiangsu Irrigation Main Canal and the estuarine area ranges from approximately 0.1 to 0.3 mg/L, while the total phosphorus concentration ranges from approximately 0.1 to 0.4 mg/L. These two water quality parameters exhibit stable concentrations in the North Jiangsu Irrigation Main Canal with minimal variations throughout the year. In the marine environment, the ammonia nitrogen concentration is higher due to the influence of freshwater runoff from rivers, resulting in lower-concentration zones in the estuarine area.

Throughout the year, the water quality in the North Jiangsu Irrigation Main Canal remains good, with a long-term water quality category of Class II. However, on 16 May, high ammonia nitrogen concentrations were observed. According to the data from the real-time monitoring system for national surface water quality, the water quality on that day was poor, with the water quality category at the Liuduo Gate Water Quality Monitoring Station being Class IV.

The water quality parameters encompass various components, such as chemical oxygen demand, total phosphorus, total nitrogen, and ammonia nitrogen, all of which are commonly used to characterize the water quality. The present study employed high-resolution remote sensing imagery to retrieve water quality parameters by developing a model specifically designed for parameter retrieval. The primary aim was to evaluate the efficacy of satellite remote sensing in estimating water quality parameters within the designated study area. Total phosphorus and ammonia nitrogen were selected as representative water quality parameters. If the feasibility of this approach is demonstrated, it could be readily applied to other parameters like total nitrogen and chemical oxygen demand, enabling the comprehensive long-term monitoring of water quality in the study area in the future.

## 5. Conclusions

Water quality parameters serve as important indicators of aquatic environments, and timely and accurate monitoring plays a crucial role in understanding the aquatic environment and protecting water quality and ecological environments. In addition to conventional field observations, satellite remote sensing has become an essential tool. In this study, total phosphorus and ammonia nitrogen were selected as indicators of water quality parameters. Through laboratory measurements of standard solutions and spectral analysis, we utilized the Sentinel-2 spectral bands to construct inversion models. Model calibration was performed using field measurements from 10 stations in the study area in 2022 and matching datasets generated by Sentinel-2, yielding applicable models for total phosphorus and ammonia nitrogen in the study area. Importantly, the models took into consideration the influence of water components, and a turbidity correction model was developed specifically for total phosphorus. Validation using an independent test dataset yielded an $R^2$ value of 0.7302 and an RMSE of 0.02614 mg/L for total phosphorus and an $R^2$ value of 0.8024 and an RMSE of 0.0368 mg/L for ammonia nitrogen. The application of the models to satellite remote sensing monitoring in the study area in 2022 provided insights into the spatial distribution and temporal variations throughout the year.

In this study, the absence of equivalent field-measured water reflectance spectra impedes direct comparisons between laboratory-measured spectra and in situ water spectra. To address this limitation, future research will involve comprehensive in situ spectral measurements. When constructing the model, it is vital to account for potential disparities between laboratory-measured spectra and in situ water surface spectra. Additionally, the inclusion of water quality parameters and in situ spectral data should be considered in order to optimize inversion models for their subsequent application to remote sensing satellite images, thus enabling long-term monitoring.

**Author Contributions:** Conceptualization, X.S. and Z.Q.; methodology, X.S. and Z.Q.; validation, X.S., Y.H. and Z.Q.; formal analysis, X.S., D.Z. and Z.Q.; investigation, X.S., A.Z. and H.L.; data curation, X.S. and Y.Z. (Yating Zhan); writing—original draft preparation, X.S.; writing—review and editing, Z.Q., Y.W. and Y.Z. (Yuanzhi Zhang); visualization, X.S.; supervision, Z.Q. All authors have read and agreed to the published version of the manuscript.

**Funding:** This research was funded by the National Natural Science Foundation of China, grant number 41976165.

**Data Availability Statement:** Restrictions apply to the availability of these data. Data was obtained from China National Environmental Monitoring Centre and are available from https://szzdjc.cnemc.cn:8070/GJZ/Business/Publish/Main.html with the permission of China National Environmental Monitoring Centre.

**Conflicts of Interest:** The authors declare no conflicts of interest.

## References

1. Zhang, Y.; Deng, J.; Qin, B.; Zhu, G.; Zhang, Y.; Jeppesen, E.; Tong, Y. Importance and Vulnerability of Lakes and Reservoirs Supporting Drinking Water in China. *Fundam. Res.* **2023**, *3*, 265–273. [CrossRef]
2. Wen, Z.; Song, K.; Liu, G.; Shang, Y.; Fang, C.; Du, J.; Lyu, L. Quantifying the Trophic Status of Lakes Using Total Light Absorption of Optically Active Components. *Environ. Pollut.* **2019**, *245*, 684–693. [CrossRef]
3. Chen, K.; Wu, L.; Zhou, H. Assessment and Trend Analysis of Water Quality in the Huaihe River Basin. *J. Hydroecol. (Chin. J. Engl. Abstr.)* **2022**, *43*, 15–21. [CrossRef]
4. Csathó, P.; Sisák, I.; Radimszky, L.; Lushaj, S.; Spiegel, H.; Nikolova, M. Agriculture as a source of phosphorus causing eutrophication in Central and Eastern Europe. *Soil. Use Manag.* **2009**, *23*, 36–56. [CrossRef]

5. Zhao, J.; Fu, G.; Lei, K.; Li, Y. Multivariate analysis of surface water quality in the Three Gorges area of China and implications for water management. *J. Environ. Sci.* **2011**, *23*, 1460–1471. [CrossRef]
6. Bangira, T.; Matongera, T.N.; Mabhaudhi, T.; Mutanga, O. Remote Sensing-Based Water Quality Monitoring in African Reservoirs, Potential and Limitations of Sensors and Algorithms: A Systematic Review. *Phys. Chem. Earth Parts A/B/C* **2024**, *134*, 103536. [CrossRef]
7. Tian, D.; Zhao, X.; Gao, L.; Liang, Z.; Yang, Z.; Zhang, P.; Wu, Q.; Ren, K.; Li, R.; Yang, C.; et al. Estimation of Water Quality Variables Based on Machine Learning Model and Cluster Analysis-Based Empirical Model Using Multi-Source Remote Sensing Data in Inland Reservoirs, South China. *Environ. Pollut.* **2024**, *342*, 123104. [CrossRef]
8. Lioumbas, J.; Christodoulou, A.; Katsiapi, M.; Xanthopoulou, N.; Stournara, P.; Spahos, T.; Seretoudi, G.; Mentes, A.; Theodoridou, N. Satellite Remote Sensing to Improve Source Water Quality Monitoring: A Water Utility's Perspective. *Remote Sens. Appl: Soc. Environ.* **2023**, *32*, 101042. [CrossRef]
9. Li, L.; Gu, M.; Gong, C.; Hu, Y.; Wang, X.; Yang, Z.; He, Z. An Advanced Remote Sensing Retrieval Method for Urban Non-Optically Active Water Quality Parameters: An Example from Shanghai. *Sci. Total Environ.* **2023**, *880*, 163389. [CrossRef]
10. Yang, W.; Fu, B.; Li, S.; Lao, Z.; Deng, T.; He, W.; He, H.; Chen, Z. Monitoring Multi-Water Quality of Internationally Important Karst Wetland through Deep Learning, Multi-Sensor and Multi-Platform Remote Sensing Images: A Case Study of Guilin, China. *Ecol. Indic.* **2023**, *154*, 110755. [CrossRef]
11. Rahat, S.H.; Steissberg, T.; Chang, W.; Chen, X.; Mandavya, G.; Tracy, J.; Wasti, A.; Atreya, G.; Saki, S.; Bhuiyan, M.A.E.; et al. Remote Sensing-Enabled Machine Learning for River Water Quality Modeling under Multidimensional Uncertainty. *Sci. Total Environ.* **2023**, *898*, 165504. [CrossRef]
12. Kowe, P.; Ncube, E.; Magidi, J.; Ndambuki, J.M.; Rwasoka, D.T.; Gumindoga, W.; Maviza, A.; de jesus Paulo Mavaringana, M.; Kakanda, E.T. Spatial-Temporal Variability Analysis of Water Quality Using Remote Sensing Data: A Case Study of Lake Manyame. *Sci. Afr.* **2023**, *21*, e01877. [CrossRef]
13. Chen, P.; Wang, B.; Wu, Y.; Wang, Q.; Huang, Z.; Wang, C. Urban River Water Quality Monitoring Based on Self-Optimizing Machine Learning Method Using Multi-Source Remote Sensing Data. *Ecol. Indic.* **2023**, *146*, 109750. [CrossRef]
14. Wu, S.; Qi, J.; Yan, Z.; Lyu, F.; Lin, T.; Wang, Y.; Du, Z. Spatiotemporal Assessments of Nutrients and Water Quality in Coastal Areas Using Remote Sensing and a Spatiotemporal Deep Learning Model. *Int. J. Appl. Earth Obs. Geoinf.* **2022**, *112*, 102897. [CrossRef]
15. Zhu, X.; Guo, H.; Huang, J.J.; Tian, S.; Xu, W.; Mai, Y. An Ensemble Machine Learning Model for Water Quality Estimation in Coastal Area Based on Remote Sensing Imagery. *J. Environ. Manag.* **2022**, *323*, 116187. [CrossRef]
16. Sedighkia, M.; Abdoli, A. Linking Remote Sensing Analysis and Reservoir Operation Optimization for Improving Water Quality Management of Reservoirs. *J. Hydrol.* **2022**, *613*, 128445. [CrossRef]
17. Mohseni, F.; Saba, F.; Mirmazloumi, S.M.; Amani, M.; Mokhtarzade, M.; Jamali, S.; Mahdavi, S. Ocean Water Quality Monitoring Using Remote Sensing Techniques: A Review. *Mar. Environ. Res.* **2022**, *180*, 105701. [CrossRef]
18. Adjovu, G.E.; Stephen, H.; James, D.; Ahmad, S. Overview of the Application of Remote Sensing in Effective Monitoring of Water Quality Parameters. *Remote Sens.* **2023**, *15*, 1938. [CrossRef]
19. Gholizadeh, M.H.; Melesse, A.M.; Reddi, L. A Comprehensive Review on Water Quality Parameters Estimation Using Remote Sensing Techniques. *Sensors* **2016**, *16*, 1298. [CrossRef]
20. Caballero, I.; Navarro, G. Monitoring cyanoHABs and Water Quality in Laguna Lake (Philippines) with Sentinel-2 Satellites during the 2020 Pacific Typhoon Season. *Sci. Total Environ.* **2021**, *788*, 147700. [CrossRef]
21. Chen, J.; Zhu, W.; Tian, Y.Q.; Yu, Q. Monitoring Dissolved Organic Carbon by Combining Landsat-8 and Sentinel-2 Satellites: Case Study in Saginaw River Estuary, Lake Huron. *Sci. Total Environ.* **2020**, *718*, 137374. [CrossRef]
22. Cao, X.; Yang, S.; Wu, P.; Liu, S.; Liao, J. Coupling Stable Isotopes to Evaluate Sources and Transformations of Nitrate in Groundwater and Inflowing Rivers around the Caohai Karst Wetland, Southwest China. *Environ. Sci. Pollut. Res.* **2021**, *28*, 45826–45839. [CrossRef]
23. Wei, L.; Wang, Z.; Huang, C.; Zhang, Y.; Wang, Z.; Xia, H.; Cao, L. Transparency Estimation of Narrow Rivers by UAV-Borne Hyperspectral Remote Sensing Imagery. *IEEE Access* **2020**, *8*, 168137–168153. [CrossRef]
24. Li, S.; Song, K.; Wang, S.; Liu, G.; Wen, Z.; Shang, Y.; Lyu, L.; Chen, F.; Xu, S.; Tao, H.; et al. Quantification of Chlorophyll-a in Typical Lakes across China Using Sentinel-2 MSI Imagery with Machine Learning Algorithm. *Sci. Total Environ.* **2021**, *778*, 146271. [CrossRef]
25. Moses, W.; Sterckx, S.; Montes, M.; De Keukelaere, L.; Knaeps, E. Chapter 3—Atmospheric correction for inland waters. Bio-optical modeling and remote sensing of inland waters. In *Bio-Optical Modeling and Remote Sensing of Inland Waters*; Elsevier: Amsterdam, The Netherlands, 2017; pp. 69–100. [CrossRef]
26. Guanter, L.; Del Carmen González-Sanpedro, M.; Moreno, J. A method for the atmospheric correction of ENVISAT/MERIS data over land targets. *Int. J. Remote Sens.* **2007**, *28*, 709–728. [CrossRef]
27. Berk, A.; Anderson, G.; Acharya, P.; Bernstein, L.; Muratov, L.; Lee, J.; Fox, M.; Adler-Golden, S.; Chetwynd, J.; Hoke, M.; et al. MODTRAN5: 2006 update. In *Algorithms and Technologies for Multispectral, Hyperspectral, and Ultraspectral Imagery XII*; SPIE: Bellingham, WA, USA, 2006; Volume 6233. [CrossRef]

28. Pereira-Sandoval, M.; Ruescas, A.; Urrego, P.; Ruiz-Verdú, A.; Delegido, J.; Tenjo, C.; Soria-Perpinyà, X.; Vicente, E.; Soria, J.; Moreno, J. Evaluation of atmospheric correction algorithms over Spanish inland waters for sentinel-2 multi spectral imagery data. *Remote Sens.* **2019**, *11*, 1469. [CrossRef]
29. De Keukelaere, L.; Sterckx, S.; Adriaensen, S.; Knaeps, E.; Reusen, I.; Giardino, C.; Bresciani, M.; Hunter, P.; Neil, C.; Van der Zande, D.; et al. Atmospheric correction of Landsat-8/OLI and Sentinel-2/MSI data using iCOR algorithm: Validation for coastal and inland waters. *Eur. J. Remote Sens.* **2018**, *51*, 525–542. [CrossRef]
30. Allam, M.; Meng, Q.; Elhag, M.; Giardino, C.; Ghirardi, N.; Su, Y.; Al-Hababi, M.; Menenti, M. Atmospheric Correction Algorithms Assessment for Sentinel-2A Imagery over Inland Waters of China: Case Study, Qiandao Lake. *Earth Syst. Environ.* **2024**, *8*, 105–119. [CrossRef]
31. Xu, H. Modification of normalised difference water index (NDWI) to enhance open water features in remotely sensed imagery. *Int. J. Remote Sens.* **2006**, *27*, 3025–3033. [CrossRef]
32. Xiong, J.; Lin, C.; Ma, R.; Cao, Z. Remote sensing estimation of lake total phosphorus concentration based on MODIS: A case study of Lake Hongze. *Remote Sens.* **2019**, *11*, 2068. [CrossRef]
33. Li, N.; Zhang, Y.; Shi, K.; Zhang, Y.; Sun, X.; Wang, W.; Qian, H.; Yang, H.; Niu, Y. Real-Time and Continuous Tracking of Total Phosphorus Using a Ground-Based Hyperspectral Proximal Sensing System. *Remote Sens.* **2023**, *15*, 507. [CrossRef]
34. Shang, W.; Jin, S.; He, Y.; Zhang, Y.; Li, J. Spatial–Temporal Variations of Total Nitrogen and Phosphorus in Poyang, Dongting and Taihu Lakes from Landsat-8 Data. *Water* **2021**, *13*, 1704. [CrossRef]
35. Wu, C.; Wu, J.; Qi, J.; Zhang, L.; Huang, H.; Lou, L.; Chen, Y. Empirical estimation of total phosphorus concentration in the mainstream of the Qiantang River in China using Landsat TM data. *Int. J. Remote Sens.* **2010**, *31*, 2309–2324. [CrossRef]
36. Du, C.; Li, Y.; Wang, Q.; Zhu, L.; Lü, H. Inversion Model and Daily Variation of Total Phosphorus Concentrations in Taihu Lake Based on GOCI Data. *Environ. Sci.* **2016**, *37*, 862–872. [CrossRef]
37. Liu, J.; Zhang, Y.; Yuan, D.; Song, X. Empirical estimation of total nitrogen and total phosphorus concentration of urban water bodies in China using high resolution IKONOS multispectral imagery. *Water* **2015**, *7*, 6551–6573. [CrossRef]
38. Cruz-Retana, A.; Becerril-Piña, R.; Fonseca, C.; Gómez-Albores, M.; Gaytán-Aguilar, S.; Hernández-Téllez, M.; Mastachi-Loza, C. Assessment of Regression Models for Surface Water Quality Modeling via Remote Sensing of a Water Body in the Mexican Highlands. *Water* **2023**, *15*, 3828. [CrossRef]
39. Zhao, J.; Jin, S.; Zhang, Y. Dynamic Water Quality Changes in the Main Stream of the Yangtze River from Multi-Source Remote Sensing Data. *Remote Sens.* **2023**, *15*, 2526. [CrossRef]
40. Dong, G.; Hu, Z.; Liu, X.; Fu, Y.; Zhang, W. Spatio-temporal variation of total nitrogen and ammonia nitrogen in the water source of the middle route of the South-to-North Water Diversion Project. *Water* **2020**, *12*, 2615. [CrossRef]
41. He, W.; Chen, S.; Liu, X.; Chen, J. Water quality monitoring in a slightly-polluted inland water body through remote sensing—Case study of the Guanting Reservoir in Beijing, China. *Front. Environ. Sci. Eng. China* **2008**, *2*, 163–171. [CrossRef]
42. Ma, F.; Gao, Z.; Ye, B. Remote sensing inversion of Tangxun lake water quality based on high score remote sensing satellite image. *Water Resour. Dev. Manag.* **2021**, *5*, 69–75. [CrossRef]
43. Wu, H.; Guo, Q.; Zang, J.; Qiao, Y.; Zhu, L.; He, Y. Study on Water Quality Parameter Inversion based on Landsat 8 and Measured Data. *Remote Sens Technol. Appl. (Chin. J. Engl. Abstr.)* **2021**, *36*, 898–907. [CrossRef]
44. Al-Shaibah, B.; Liu, X.; Zhang, J.; Tong, Z.; Zhang, M.; El-Zeiny, A.; Faichia, C.; Hussain, M.; Tayyab, M. Modeling water quality parameters using landsat multispectral images: A case study of Erlong lake, northeast China. *Remote Sens.* **2021**, *13*, 1603. [CrossRef]
45. Zhou, C.; Jiao, X.; Mao, C.; LÜ, Y.; Zhang, P. Present Marine Environment Situation Investigation in the Nearshore Area of Guanhe Estuary in Spring. *J. Guangdong Ocean. Univ. (Chin. J. Engl. Abstr.)* **2018**, *38*, 27–34. [CrossRef]